Journal of
Materials Chemistry A

Accepted Manuscript

Preparation, Structure and Electrochemistry of $LiFeBO_3$: a Cathode Material for Li-ion Battery

L. Tao[a], G. Rousse[b], J.N. Chotard[a], L. Dupont[a], S. Bruyère[a], D. Hanžel[c], G. Mali[d,e], R. Dominko[d], S. Levasseur[f] & C. Masquelier[a]*

[a] Laboratoire de Réactivité et de Chimie du Solide (LRCS), CNRS UMR7314, Université de Picardie Jules Verne, 33 rue Saint Leu, 80039 Amiens, France

[b] Institut de Minéralogie et de Physique des Milieux Condensés (IMPMC), Université Pierre & Marie Curie UPMC Univ Paris 06, CNRS UMR7590, 4 Place Jussieu, 75252 Paris Cedex 05, France

[c] Institute Jožef Stefan, Jamova 39, SI-1000 Ljubljana, Slovenia

[d] National Institute of Chemistry, Hajdrihova 19, SI-1000 Ljubljana, Slovenia

[e] EN-FIST Centre of Excellence, Dunajska 156, SI-1000 Ljubljana, Slovenia

[f] Umicore, Broekstraat 31, 1000 Brussels, Belgium

Corresponding author at christian.masquelier@u-picardie.fr

ABSTRACT

Li*M*BO_3 (*M* = Fe, Co, Mn) has been identified as an interesting new cathode material for Li-ion batteries. It was shown to be difficult to synthesize as a pure phase and in a highly-electrochemically-active form. Here we report several methods for the successful preparation of $LiFeBO_3$, including traditional ceramic and self-combustion reactions. By decreasing particle size and introducing in-situ carbon coating, conventional ceramic-synthesized $LiFeBO_3$ yields a first discharge of 210 mAh/g within the 1.5–4.5V voltage window at C/20 rate, 55^{o}C. Using high-resolution synchrotron X-ray diffraction, neutron powder diffraction and single crystal X-ray diffraction in combination with ^{6}Li NMR and ^{57}Fe Mössbauer spectroscopies, we present a "1Fe 2Li" complex cation distribution model for $LiFeBO_3$ powder.

Keywords: Borates, Cathode, Li-ion Battery, Crystal Structure

1 Introduction

For the past two decades, Li-ion batteries have become ubiquitous in modern society, from personal electronic devices to automotive vehicles. The discovery and development of polyanionic materials as Li^+ insertion/extraction electrodes, such as *olivine*-type $LiFePO_4$ [1, 2] has paved the way for alternative chemistries and improved materials for Li batteries [3]. Recently, iron-based compositions such as silicates [4-6], borates and fluorosulfates [7-9] received a significant amount of attention. Investigations into the transition-metal borate phases have principally focused on compounds like *calcite*-type $FeBO_3$ [10, 11] and VBO_3 [12], *norbergite*-type Fe_3BO_6 [10, 11] Cr_3BO_6 [13], and *kotoite* $(Co,Ni,Cu)_3B_2O_6$ [14]. Unfortunately, extremely large cell polarizations resulting from poor electrical conductivity and conversion-type electrochemical reaction with Li^+ generate a low operating voltage on discharge (~1V vs. Li^+/Li^0) and hinder their practical use in Li-ion batteries. Indeed, it was not until 2001 when Legagneur *et al.* [15] first published the successful preparation of Li*M*BO_3 (*M* = Fe, Co, Mn) that transition-metal borates drew a significant amount of attention from the battery community. Unfortunately, while these phases were found to be electrochemically active, less than 0.04 Li^+ per formula unit could typically be removed in these early studies. Nevertheless, the high theoretical capacity of $LiFeBO_3$ (220 $mAh.g^{-1}$, i.e. 30% higher than $LiFePO_4$) generates among the highest theoretical energy densities of polyanionic materials: 613 $Wh•kg^{-1}$ vs. 586 $Wh•kg^{-1}$ for $LiFePO_4$ and 655 $Wh•kg^{-1}$ for $LiVPO_4F$ [16, 17].

Attempts to improve the reversible electrochemical capacity of $LiFeBO_3$ have been reported only very recently. Early studies involving carbon coating were first pursued by Allen *et al.* [18] as well as by Abouimrane *et al.* [19] and succeeded in increasing the capacity to almost 140 $mAh.g^{-1}$ when cycled at 80°C. More recent work by the groups of Yamada [20, 21] and Khalifah [22] reported on almost full experimental capacity of $LiFeBO_3$ (190 $mAh.g^{-1}$) on electrochemical cycling, despite the presence of around 10 wt% of Fe_3BO_5 impurity. The group of Yamada [20] demonstrated that moisture in air is detrimental to the Li (de)insertion process due to what appeared as a surface contamination of the particles. This surface degradation was later confirmed and more thoroughly characterized as a function of time and particle size by Bo *et al.* [22]. Both studies highlighted the importance of carbon coating to enhance the electrical conductivity, a need for very small particles to minimize the diffusion length, and the necessity to maintain a carefully controlled atmosphere free of air and moisture in order to access the maximum capacity.

Crystals of Li*M*BO_3 (*M* = Fe, Mn, Co) are most commonly found to crystallize in the monoclinic space group *C*2/*c*, but a hexagonal (*P*-6) polymorph of $LiMnBO_3$ [15, 23-27] also

exists. Several structural models have been used to describe the average structure of the monoclinic phase of $LiFeBO_3$. The original structure proposed by Legagneur [15] from single crystal X-Ray diffraction identified two partially occupied Fe sites and two partially occupied Li sites. Yet further work by Yamada [20], which used laboratory X-Ray powder diffraction in combination with ^{57}Fe Mössbauer spectroscopy, suggested that only one crystallographic site exists for Fe and Li. Most recently, a re-examination of single crystal diffraction by Khalifah's group [28] identified a commensurate modulation of the Li positions in the structure.

In order to ensure an accurate structural analysis as well as good battery performances, high-purity $LiFeBO_3$ powders were prepared using a wide variety of techniques to minimize the presence of impurities and (or) to coat a homogenous conductive carbon layer. Further, to gain insight into the complex electrochemical performance of $LiFeBO_3$ when used as a positive electrode in Li ion batteries, we have re-examined its crystal structure using high-resolution synchrotron X-Ray diffraction data, neutron powder diffraction and single crystal X-ray diffraction in combination with ^{57}Fe Mossbauer and ^{6}Li-NMR. Single crystals were picked out directly from the powder made for battery appliances and were analyzed to compare the differences between powder and crystal. Last, we present the electrochemical properties of this material and the use of *in-situ* X-ray measurement so as to probe the Li^+ insertion / extraction mechanism.

2. Synthesis and materials characterization

Polycrystalline Li*M*BO_3 (*M* = Fe, Mn, Co) is usually prepared through traditional ceramic routes using *M*$C_2O_4 \cdot 2H_2O$, Li_2CO_3, $LiOH \cdot H_2O$, $LiBO_2$, B_2O_3 or H_3BO_3 as the most common precursors.

Ceramic Preparation:

● Non carbon coated: Iron(II) oxalate dihydrate ($FeC_2O_4 \cdot 2H_2O$, 99% Alfa Aesar), boric acid (H_3BO_3, 99.5% Alfa Aesar) and lithium hydroxide monohydrate (LiOH, 98% Aldrich) were ball milled in acetone for 1 hour and dried prior to a heating to 300^{o}C under a flow of Ar for four hours. The resulting amorphous black powder was subsequently pressed into 13 mm pellets and heated up to 600^{o}C for 10 hours under Ar. The sintered pellet was then immediately placed in an Ar-filled glove box and ground into a powder of ~20 μm individual particles before further characterization.

● Carbon coated: Ascorbic acid (99% Aldrich) was ball milled together with precursors used for non-carbon coated $LiFeBO_3$ in an Ar-filled stainless steel jar for 30 minutes prior to be dried at 90°C for another 30 minutes in a vacuum drier. The resulting grass-green blocks were immediately ground into powder by mortar before being transferred into a tube furnace heated up to 600°C for 10 hours under a mixed CO/CO_2 (volume ratio 3:7) gas flow. The as prepared fine black powder was transferred to the Ar-filled glove box once taken out.

Self-Combustion Preparation: In order to reduce the particle size and to initiate a carbon coating, a self-combustion procedure was also utilized [29, 30]. To this end, 3.52 g of citric acid (99.5% Alfa Aesar), 1.80 g ascorbic acid (99% Aldrich), 0.995 g $LiBO_2$ (99.9% Alfa Aesar) and 8.08 g $Fe(NO_3)_3 \cdot 9H_2O$ (98% Alfa Aesar) were stirred and dissolved in 40 ml of distilled water. The solution continued to stir on a hot plate as the mixture was heated to 110°C to trigger a reaction in which a red-brown smoke was generated. After approximately 10 minutes a dry, amorphous, brown residue was collected. This residue was ground in a mortar and heated up to 600°C in Ar for 1 hour to produce porous carbon-coated $LiFeBO_3$ as revealed by TEM.

Room temperature Powder X-ray diffraction (XRD) patterns were collected using two separate Bruker D8 laboratory diffractometers with either $Cu_{K\alpha}$ or $Co_{K\alpha}$ radiation. After evaluating the purity of the powders, selected samples were sealed inside 0.5mm diameter glass capillaries, and sent to the 11-BM beam line at the APS Argonne, USA, for high resolution synchrotron X-ray diffraction data acquisition. To this end, a constant wavelength of 0.4131 Å was used in the 2θ range 1°-50°, with a step size of 0.001°.

Neutron diffraction data was acquired on powder (~2g), constrained in an 8mm diameter vanadium tube, using the high resolution diffractometer D2B of the Institut Laue Langevin (ILL Grenoble France) in transmission mode at room temperature. To this end, a constant wavelength of 1.594 Å was used in the 2θ range 1°-160°, with a step size of 0.05°, accumulated for about 9 hours. ^{7}Li and ^{11}B isotope rich precursors were used in preparation of the $LiFeBO_3$ [31] to avoid severe neutron absorption.

All powder diffraction patterns were refined using the Rietveld method [32] as implemented in the FullProf suite [33].

Rod-like light grey transparent $LiFeBO_3$ single crystals of dimension ~25×25×75 μm were directly picked out from the powder prepared via the ceramic route. The single crystal X-ray diffraction data were recorded with a Bruker D8 Venture diffractometer equipped with a

MicroSource X-ray generator using the $Mo_{K\alpha}$ (0.71073 Å) radiation at 298 K operating at 50 KV and 1200 μA. Data reduction and absorption corrections were carried out within the software APEX II. Structure solution was solved using SHELXS97 [34] while ShelXle [34] was used for the structure refinement.

Scanning Electron Microscopy (SEM) coupled with Energy dispersive X-ray spectroscopy (EDS) was used to determine the sample morphology and chemical composition. Samples for Transmission Electron Microscopy (TEM) were dispersed in acetone and then a few drops were deposited on a holey nickel grid. The TEM images, electron diffraction patterns and the energy disperse X-ray spectra were obtained using a FEI Tecnai F20 S-TWIN operating at 200 kV.

^{6}Li MAS (magic angle spinning) NMR spectra were recorded at ^{6}Li Larmor frequency of 88.35 MHz on a 600 MHz Varian spectrometer (14.1T) with the rotation-synchronized Hahn-echo pulse sequence. The frequency offsets were selected after an experimental inspection of the excitation profile of the echo pulse sequence. The offsets -100 kHz, 0 and 100 kHz guarantee that the sum of the corresponding three sub-spectra yields a spectrum that is undistorted over the 200 kHz broad central region. The duration of the π/2 pulse was 2μs, the sample rotation frequency was set to 35.7 kHz and the repetition delay between consecutive scans was 0.25s for a total number of scans of 300000. The spectra were obtained as sums of three sub-spectra, recorded by using three irradiation frequencies (central frequency of 88.35 MHz and two that were offset by ±100 kHz). Frequency axis (in ppm) is reported relative to the lithium signal of a 1M LiCl solution.

The absorber for Mössbauer measurements was prepared inside a glove box in dry Ar atmosphere from ground $LiFeBO_3$, mixed with BN and put into a sample holder which was sealed with glue to avoid any air and moisture contact during measurements. The source is Co^{57} in rhodium, and the spectra were measured both at room temperature and at 70K with a constant acceleration. In prior to measurement, the equipment was calibrated with α-Fe foil reference.

Electrochemical tests were carried out vs. Li either using Swagelok or coin cell type configurations with a Macpile or a VMP system (Biologic S.A., Claix, France). For Swagelok type cells, the $LiFeBO_3$ powder was ball milled with 20% in mass of Carbon SP for 20mins. Usually ~5mg of active material was scattered on current collector per cell. For coin type cells, carbon coated $LiFeBO_3$, Carbon Black and PVDF-HFP in weight ratio 70/20/10 were magnetic-stirred in acetone for 12 hours before casted on a clean Al foil. After the

evaporation of the acetone, the casted electrode was immediately transferred into Buchi Oven, dried at 110°C for 2 hours. The punched electrodes of diameter ~11mm were stored in glove box for further characterizations. A Whatman GF/D borosilicate glass fiber separator was chosen for the two types of cells mentioned above, saturated with 1M $LiPF_6$ in ethylene carbonate (EC) and dimethyl carbonate (DMC) (1:1 w/w) electrolyte (Merck LP30). All the cells were assembled in an argon-filled glove box, using Li metal disk as the negative electrodes. Galvanostatic charge-discharge tests were conducted.

In-house *in situ* XRD patterns were recorded with a Bruker D8 Advance AXS diffractometer using the CuK_α radiation. The special designed stainless steel *in situ* cell [35] was assembled in Ar-filled glove box, using Li anode, LP30 electrolyte and ~ 30 mg $LiFeBO_3$/C cathode similar to what has been described for Swagelok type. A thin Al foil (3 µm) was used behind the beryllium window to prevent from its possible oxidation at high voltages. The diffraction peak of Al (at $2\theta_{CuK\alpha}$ = 38.6°) was used as a position reference for successive experiments. Typically the cell was cycled at C/50 rate meanwhile XRD patterns were collected every 2 hours for a 10°-40° 2θ range.

3 Results and Discussion

Preparation:

The preparation of completely pure $LiFeBO_3$ is non-trivial and typical secondary phases include Fe_3BO_5 (Fe^{2+}/Fe^{3+} mixed valence compound), $Li_2Fe_3O_4$ and elemental Fe. The upper XRD pattern of Figure 1a is a representative result for many of the samples obtained and is comparable to the data reported by Yamada *et al.* [20, 21] and Bo *et al.* [22], who typically found roughly 10% by mass of Fe_3BO_5 in their samples. We have found that the key variable for the successful preparation of pure $LiFeBO_3$ is a very careful control of the surrounding atmosphere at all stages of the procedure: while mixing the precursors, ball-milling, drying, all the way through the annealing stage. Under these dry conditions, phase-pure and well-crystallized particles of $LiFeBO_3$ with typical particle diameters on the scale of ~20 µm were obtained *via* the ceramic route, as shown in Figure 1b. It is especially important to avoid any oxidation of Fe^{2+}, which occurs spontaneously in H_2O and O_2-containing environments. Dong *et al.* [23] achieved these conditions by using a reducing 5% H_2/Ar flow during the annealing step at 650°C in order to compensate for any partial oxidation of Fe^{2+}. On the other hand, we observed that exposing $LiFeBO_3$ with reducing gases Ar/H_2 (10%) even at moderate temperatures (~600°C) could yield powders with significant amounts of Fe metal. Instead, we found that a flowing mixture of CO/CO_2 provides the best control of the iron oxidation state in

addition to offering a promising way of carbon coating through decomposition of ascorbic acid.

Crystal Structure of $LiFeBO_3$

● *Synchrotron X-ray Diffraction*

Figure 2 shows our room-temperature high-resolution synchrotron X-Ray diffraction data, with the insets illustrating the clear separation of the diffraction peaks (FWHM = 0.008° at 2θ = 10°) when compared with a laboratory source. Pattern matching refinements revealed that all of the diffraction peaks (with the exception of small intensity ones, corresponding to 0.5 wt% of Fe^0) may be indexed in the *C2/c* monoclinic unit-cell previously given in the literature [15], with a = 5.1701(1) Å, b = 8.9219(2) Å, c = 10.1656(2)Å, β = 91.443(1)° and V = 468.76(1) $Å^3$.

The Rietveld [32] refinements of the structure from the Synchrotron XRD data were performed starting from the structural model obtained using direct methods as implemented in the EXPO [36] software package. This starting model yielded essentially the same as what Yamada had reported, with space group *C2/c*. In all reported structures, including this study, $LiFeBO_3$ is comprised of chains of edge-sharing [FeO_5] trigonal bipyramids running along [-101] that stack perpendicular to the [010] direction (see Figure 3a). As this is a polyanionic compound, it is important to note that all of the oxygen atoms within the structure are bound to trigonal planar BO_3 units. The model was improved by successive modifications, each of them tested step by step by Rietveld refinements and either kept or rejected based on whether the change improved the fit to the data.

Attempts to refine the structure from the simplest model of Yamada with only one site for both Li and Fe typically yielded unreasonably large B_{iso}(Li) values in excess of 5 $Å^2$ and hence suggested the possibility that the Li site was actually split into several positions. Difference Fourier maps (GFourier software within FullProf suite) were calculated to examine the agreement between the distribution of electron density and the integrated intensities observed in the experimental pattern while only taking into account the host structure $Fe_{8f}B_{8f}[O_{8f}]_3$. Indeed, two split maximum electronic densities residues at (0.335, 0.497, 0.345) & (0.357, 0.493, 0.412) were found in the vicinity of the Li atom position at (0.354, 0.498, 0.371), as shown in Figure S1. The examination of these coordinates revealed that the site splitting mostly occurs along [001] at a distance of roughly 0.7 Å (Figure 3d). Subsequently, Rietveld refinements were conducted in order to confirm or reject these findings and converged towards a clear separation of two Li crystallographic sites with respective

occupancies of 0.39(3) (Li(1)) and 0.60(3) (Li(2)). Global agreement factors (R_{Bragg}=6.70%) were significantly improved and the values of the atomic displacement parameters of Li(1) and Li(2) converged towards stable values of B_{iso}=0.63(4) Å^2 and B_{iso}=1.73(7) Å^2, respectively. A similar global procedure was applied for the atomic position(s) of iron. Contrary to what is found for Li, both Fourier difference maps and refinements of anisotropic thermal motion parameters lead to one crystallographic site for Fe (0.164, 0.332, 0.121) (Figure. 3c). Thus, we find that the most appropriate description of the average structure of $LiFeBO_3$ consists in two positions for Li which have roughly equal occupancies and only a single site for Fe within a slightly elongated ellipsoid. Bond Valence Sums were calculated using the Zachariasen formula [$V_i=\Sigma_j s_{ij}=\Sigma\exp\{(d_0-d_{ij})/0.37\}$] with the parameter d_0, which characterizes a typical cation-anion distance, taken from Brown *et al.* [37]) for Fe, B, Li(1) and Li(2) and were respectively found as 1.88, 3.03, 1.01 and 1.00, in good agreement with the expected valences. The crystallographic data and global agreement factors can be found in Table S1.

● *Neutron Powder Diffraction*

In order to confirm our complex cation distribution model, particularly the Li disorder, Rietveld refinements of room temperature neutron data was carried out. Similar to what had been done from the synchrotron X-ray diffraction data, difference Fourier maps (GFourier software within FullProf suite) were calculated to examine the agreement between the distribution of nuclear density and the integrated intensities observed in the experimental pattern while only considering the host structure $FeBO_3$. Again, two split maximum residual nuclear densities (0.316, 0.496, 0.342) & (0.345, 0.494, 0.413) were found in the vicinity of the Li atomic position of Yamada's model. The result is in good agreement with the electronic residual densities (0.335, 0.497, 0.345) & (0.357, 0.494, 0.413), found by running difference Fourier map of synchrotron X-ray data while only taking the host structure into account. On contrary to Li, the Fourier difference map by taking the host structure of [$LiBO_3$] into account lead to a single Fe site besides the shape of the nuclear residue in good agreement with the shape of the refined Fe ellipsoid (Figure S2). Our complex cation distribution model ('2Li 1Fe') proposed by synchrotron X-ray Rietveld refinements was confirmed by the neutron powder diffraction data, for which we followed the same procedure of successive difference Fourier maps. The resulting structure leads to good global agreement factors: R_{Bragg} =5.38%, R_f =3.11%, R_{wp} =4.40%, R_p =3.45% (see Figure 4 and Table 1). Besides, calculated bond valence sums using the Zachariasen formula ($V_i=\Sigma_j s_{ij}=\Sigma\exp\{(d_0-d_{ij})/0.37\}$ using the parameters d_0, characterizing a cation-anion pair, has been taken from [37]) for Fe, B, Li(1) and Li(2) were respectively found as 1.98, 2.88, 1.02 and 1.03, in extremely good agreement

with the expected valences. Further, the degree of the structural distortion of each LiO_4 tetrahedra (calculated using the formula $\Delta = 1/4\ \Sigma_{n=1,4}\{(d_n - \langle d \rangle)/\langle d \rangle\}^2$, where, d_n are the individual Li-O distances and $\langle d \rangle$ is the average value of the 4 Li-O distances) is similar for both $Li(1)O_4$ ($\Delta=1.79\times10^{-3}$) and $Li(2)O_4$ ($\Delta=6.00\times10^{-3}$).

● *^{6}Li NMR*

To complement the high-resolution synchrotron and neutron diffraction data, NMR investigations were carried out to gain insight into the appearance of the two distinct crystallographic sites for Li. In principle, ^{6}Li MAS NMR spectroscopy is capable of detecting even minor differences in the coordination environment of Li and thus offers an invaluable tool for the study of insertion electrodes [38]. The ^{6}Li MAS NMR spectrum of $LiFeBO_3$ is presented in Figure 5a. The line-width (FWHM) of the centre-band and the sidebands is around 110 ppm, which is rather broad, even for an Fe^{2+} containing compound especially when compared with the FWHM of 60-70 ppm observed for Li_2FeSiO_4 polymorphs [39]. This abnormally broad line-width suggests the existence of two overlapped contributions; however, the centre- and side-bands appear relatively symmetrical as in the work of Bo [22], who argued for the existence of a single resonance peak with an isotropic shift of -233 ppm. On the other hand, taking into account that Li(1) and Li(2) environments are very similar in our structural model and that ^{6}Li NMR signals are inherently broad in Fe^{2+} containing materials due to the anisotropic bulk magnetic susceptibility effect [39-42], it is not unreasonable to expect that the apparent symmetrical ^{6}Li NMR signals are actually a sum of two severely overlapped contributions. Unlike the case of the $P2_1/n$ phase of Li_2FeSiO_4 [39], the $Li(1)O_4$ and $Li(2)O_4$ tetrahedra in $LiFeBO_3$ are both corner-shared with 4 FeO_5 trigonal bipyramids and edge-shared with 1 FeO_5 (see Figure 3d). Further, the structural distortion of each LiO_4 tetrahedra (Δ) was found similar from neutron diffraction, and the average Fe-Li(1) distance (5 closest Fe) is 3.026 Å, while the average Fe-Li(2) distance is 3.043 Å. Thus, while two ^{6}Li signals are expected, there should be only little difference in the isotropic positions as well as in their spinning-sidebands powder patterns.

To better resolve the issue of the peak broadness, the isostructural phase $LiMnBO_3$ (phase pure sample prepared in ceramic method) was also investigated since the signals of the Mn^{2+} containing material are expected to be much narrower than those of the Fe^{2+} containing material. Indeed, as shown in Figure 5b, the center-band and sidebands within the ^{6}Li MAS NMR spectrum of $LiMnBO_3$ are clearly asymmetrical, and the spectrum can be fitted very well using two separate contributions with only slightly different isotropic shifts (δ(Li1) = -194

ppm, δ(Li2) = -209 ppm and line-width ~ 20 ppm). The analysis of isostructural $LiMnBO_3$ provides some justification for an attempt to decompose the ^{6}Li MAS NMR spectrum of $LiFeBO_3$ into two contributions. An attempt which uses two contributions with Gaussian line shapes yields the following isotropic positions and integrated intensities: δ(Li1) = -234 ppm, 66%, and δ(Li2) = -221 ppm, 34%. The obtained ratio of the intensities of the two Li contributions is satisfactory agreement with the occupancies of the two Li sites within our $LiFeBO_3$ crystal structural model.

● *^{57}Fe Mössbauer spectroscopy*

Having examined the nature of the Li site, ^{57}Fe Mössbauer was employed to examine the environment of Fe in the structure. A room temperature, magic angle ^{57}Fe Mössbauer spectrum was collected for two weeks and compared with a pattern which was collected at a lower temperature of 70 K. The Mössbauer spectra collected on the as-prepared $LiFeBO_3$ (consistent for three types of synthesis) showed unambiguously the presence of two Fe^{2+} doublets. If there were truly only one crystallographic site for Fe, there would be no way to produce a signal with two unique environments. Thus, it first appears as though the Mössbauer and NMR data supports the model of Legagneur. However, this does not prove to be the case. A closer inspection of the spectra, illustrated in Figure 6, reveals that two symmetrical Fe^{2+} doublets are not actually sufficient to fit the data, as determined form the unreasonably large residual difference curve in the long acquisition-time spectrum which should be exempt from particle morphology since it was collected using the magic angle technique. In fact, the best fit to the data was obtained by using at least four different doublets for Fe^{2+}, one doublet for Fe^{3+} to account for a small amount of surface oxidation, and one sextet for the tiny Fe^0 impurity seen in the XRD patterns. The results of this fit can be found in Figure 6a and Table S2. The chemical shifts for all four Fe^{2+} doublets are around 1mm/s with distributed quadrupolar splitting. The 70K spectrum had to be fit with multiple similar Fe^{2+} doublets as well (see Figure 6b); however, the population of the similar Fe^{2+} doublets changed significantly at lower temperature. The result of Mössbauer is consistent with our model, considering the thermal motion of Fe atoms within the slightly elongated-shaped ellipsoid. Further, the fact that Mössbauer data had to be fitted with multiple Fe^{2+} environments raised up our interests towards the recently reported commensurate modulated superstructure of $LiFeBO_3$ [22] which will naturally generate 4 Fe^{2+} environments by modulation along the **a**-axis.

● *Single Crystal X-ray Diffraction*

In order to verify / discuss / confront our ('2-Li 1-Fe') model with those published in the literature, we additionally performed single crystal X-ray diffraction (using MoK_α radiation) on $LiFeBO_3$ crystals (~25×25×75 μm) collected from powder. Two sets of measurements recorded on exactly the same crystal and their corresponding h0l diffraction data are presented in Figure 7. From the right photograph barely any satellite reflections corresponding to the modulation vector (1/2 0 0) [28] could be observed even though the collection time was somehow a standard one for single crystal structure determination. Only if the exposure time had been extended up to 10 times longer, that is 300 seconds per image, superstructure weak reflections could be observed, as indicated on the left-hand side of Figure 7. Similar measurement setups were applied to a few other crystals, and although extremely weak, the superstructure reflections generated by the modulation could be observed in "good" crystals. However, they are so weak that the recorded data from crystals even slightly less perfect won't present such satellite reflections. We therefore decided to solve the crystal structure of $LiFeBO_3$ by using only the diffraction spots related to the "standard" *C*2/*c* unit-cell of $LiFeBO_3$, i.e. same as for the powder data description described above. The solution we propose here and that proposed by Khalifah et al. account for multiple Li^+ and Fe^{2+} environments, spotted by ^6Li NMR and ^{57}Fe Mössbauer experiments. The single crystal XRD data were refined using structure-invariant direct method for primary atom sites and using difference Fourier maps for the secondary atom site locations. Without considering the modulation, we always found two Li sites (d(Li1-Li2)~0.66 Å) with respective occupancies of 47 / 53, i.e. in excellent agreement with the results of neutron data Rietveld refinements, yielding very good global agreement factors as indicated in Table S3. It is important to note that the Li1-Li2 sequence arises along the [001] direction, perpendicular to [100] and is fully consistent with the modulation vector along [100] discovered by Khalifah et al. [28]. Additionally, and again fully consistent with our neutron diffraction data and the modulation found by Khalifah, the oxygen O(3) displays strong anisotropic thermal motion factors, with the ellipsoid elongated along [001] (Table S3). To summarize, the *C*2/*c* description of the crystal structure of $LiFeBO_3$, which is the only one to be possibly observed from powder diffraction data, can be very precisely described as an average model of the modulated superstructure observed in rare cases in crystals.

● *Structure vs. Electrochemical Properties*

As mentioned earlier, $LiFeBO_3$ is built up by edge-sharing FeO_5 trigonal bipyramids ribbons connected via BO_3 triangular units, while the Li atoms are located in a zigzag shaped channel along the **c**-axis (Figure S3). Through first-principles calculation [26, 28], Li^+ ions were found to diffuse most probably along the zigzag channel (1D) with the a lowest

activation barrier energy of ~450 meV. Therefore, $LiFeBO_3$ may be sensitive to the presence of defects in the diffusion channel, as suggested for other 1D materials [43]. This is probably the reason why micro-sized $LiFeBO_3$ are almost electrochemically inactive even with a conductive carbon coating. Furthermore, O(3) atoms are in the same plane as Li atoms with large thermal motions, as indicated by the ellipsoid of O(3) visualized in Figure S3. The strong modulation / thermal motions of O atoms might hinder the Li^+ diffusion within the material and therefore resulting in even poorer electrochemical properties, as suggested by Grey and Khalifah [22].

Like $LiFePO_4$, $LiFeBO_3$ is an intrinsically poor conducting (3.9×10^{-7} S/cm [44]) material. Hence it is important to decrease the particle size of the active material (so as to shorten the Li^+ diffusion path) as well as to coat them with a conductive carbon layer (so as to improve electronic conductivity) [20, 22, 23].

It is noted that all the crystal structural characterizations were carried out on the non-carbon coated ceramic-prepared highly crystalline $LiFeBO_3$. Meanwhile we don't observe significant structural changes on the carbon coated electrochemically reactive $LiFeBO_3$/C samples, as indicated by Figure S4.

Electrochemistry:

The specific capacity of $LiFeBO_3$ obtained during Li-ion extraction/insertion is dependent on the synthesis routes which will result in different morphology, particle size as well as conductive carbon-coatings.

Figure 8 shows the morphology of two illustrative samples, and their electrochemical performances using Swagelok-type cell configurations. Sample (**A**) (used for crystal structure determination) prepared by ceramic annealing without the addition of carbon source consists of highly crystalline, ~20 μm big particles of $LiFeBO_3$. Its corresponding electrochemistry illustrates well the inherent limitations of $LiFeBO_3$. Sample (**B**) was prepared by the self-combustion technique which gave rise to a porous framework containing many agglomerated small crystallites (~50 nm) as evidenced by SEM and TEM (inset) and 20% of carbon produced by the thermal decomposition of the citric acid fuel. The $LiFeBO_3$ crystallites size of ~ 440(90) Å obtained from full-pattern matching refinements (Figure S5) is in good agreement with microscopic observations. Consequently, this sample showed much better electrochemical response, and could deliver ~0.8 Li^+ per formula unit (176 mAh/g) at C/50 rate at 298 K, during the first discharge from 4.3 V to 1.5 V vs. Li. The excess amounts of

carbon in sample (**B)** (~20 wt%) sacrifice the tap density of the material, and therefore a sample with less carbon, electrochemically active $LiFeBO_3$/C was prepared (Sample **C**).

Sample (**C**) consists of small carbon-coated particles of $LiFeBO_3$ (prepared via an insitu carbon-coating ceramic route at 600°C through the decomposition of ascorbic acid, containing ~8 wt% carbon) and shows superior electrochemical properties at 55°C (Figure 9) with small polarization, excellent reversibility and a well-defined redox activity of the Fe^{3+}/Fe^{2+} redox couple at 2.8 V vs. Li. When cycled down to 1.5 V vs. Li, this sample delivers a capacity of 210 mAh/g, i.e 95 % of the theoretical capacity of $LiFeBO_3$, with noticeably, 20 % of this capacity being delivered at ~1.8 V *vs.* Li. This has been previously reported in the literature [20, 22] and attributed to a "conversion-like reaction" of $LiFeBO_3$ involving the reduction of Fe^{2+} into Fe^0 and possibly the reduction of the Fe_3BO_5 impurities in the sample.

We have run parallel experiments in order to try to reveal the influence of the low voltage cutoff value (1.5 V vs. 2 V) on the reversibility of the reaction. As indicated by Figure S1, under the same battery cycling conditions (temperature, cell assembling, and charge/discharge rate) $LiFeBO_3$/C demonstrated divergent electrochemical responses vs. Li depending on the discharge cutoff voltage. When the cells were tested down to 1.5 V vs. Li for increased number of cycles, it was found that instead of a continuous capacity fade, the as recorded specific capacity of $LiFeBO_3$ went up, reached full theoretical capacity (220 mAh/g) at the 50^{th} cycle (1^{st} discharge ~170mAh/g) and even reached capacities as high as 350mAh/g (1.6 times of the theoretical capacity of $LiFeBO_3$) for the 70^{th} cycle, probably due to reactivity with the electrolyte at low voltage. Therefore, it is recommended to fix the voltage limit on discharge at E > 2V vs. Li and under these conditions we are able to demonstrate here (although the reached capacity is ~155 mAh/g) an excellent cyclability, as depicted in Figure 10.

Thanks to the satisfactory electrochemical properties of our samples, we were able to perform in situ X-Ray diffraction experiments during charge (~0.75 Li^+ per formula extraction) and subsequent discharge (0.70 Li^+ per formula insertion) of $LiFeBO_3$ at RT, shown in Figure S7. When the Li/$LiFeBO_3$ cell was being charged, a gradual shift in the position of the peaks towards higher 2θ angles was identified. Subsequently a gradual shift in the position of the peaks towards lower 2θ angles was observed during the discharge step. As indicated by Figure S7 (discharge until 2.0 V vs. Li^+/Li) and Figure S8, $LiFeBO_3$ demonstrates high electrochemical reversibility towards extraction / insertion of lithium. The gradual peak shift seems to support a solid solution Li^+ extraction / insertion mechanism from / into $LiFeBO_3$

[20]. On the other hand, Khalifah and Grey [22] proposed a two phase mechanism occurring at least partially (during charge / discharge), evidenced by GITT measurements. Unfortunately, our electrochemically reactive $LiFeBO_3$/C (sample **C**) is less crystalline than the non-carbon coated $LiFeBO_3$ (sample **A**). Besides, a ball milling process in the electrode preparation can decrease the crystallinity of $LiFeBO_3$, preventing us from revealing the exact Li^+ insertion mechanism through *in-situ* XRD experiments. Even with the *ex-situ* XRD patterns recorded for 12 hours (2θ range 15^o-40^o, step size of 0.015^o), we could not reach a concrete conclusion. More precise measurements are demanded.

Conclusion

We have reported on several successful routes for the preparation of $LiFeBO_3$ using ceramic processing as well as self-combustion techniques with or without carbon coating. The obtained powders of $LiFeBO_3$ were analyzed by high quality synchrotron X-ray diffraction, neutron powder diffraction, ^{6}Li NMR, ^{57}Fe Mössbauer and single crystal X-ray diffraction. We proposed an average "1Fe 2Li" structure model for $LiFeBO_3$ powder, where Li atoms partially occupied two split sites and Fe atom randomly located within a slightly elongated ellipsoid. This model is consistent with the modulated superstructure model and could be considered as an averaged, less ordered situation of the commensurate modulated superstructure model observed in some single crystals.

We had obtained homogenous carbon-coated nano-sized $LiFeBO_3$/C through ascorbic acid decomposition, which could deliver 210 mAh/g reversible capacity cycled at 55^oC C/20 rate within 1.5-4.5V in coin-type cell configuration. But the discharge below 2V is probably due to the conversion reaction. Therefore the 2.0 V cutoff voltage is recommended and using this cutoff voltage, $LiFeBO_3$/C could reversibly deliver ~155 mAh/g capacity at C/20 rate 55^oC with good capacity retention up to 50 cycles. Through *in-situ* XRD measurements, despite repetitive careful experiments, the mechanism of Li^+ insertion / extraction into $LiFeBO_3$ remains unclear. In order to fully understand the reaction, even more accurate characterizations are needed.

Acknowledgements

We acknowledge the Centre National de la Recherche Scientifique (CNRS) and UMICORE (Belgium) for the PhD Grant of L.T. The authors thank Prof. Jean-Marie Tarascon and Dr. Nadir Recham for helpful discussions. The authors thank B. Melot, T. McQueen & J. Neilson for PDF and magnetic investigations (not shown here) and useful discussions. The authors

thank Dr. Thomas C. Hansen and ILL-Grenoble for help with collection of neutron diffraction data. Use of the Advanced Photon Source at Argonne National Laboratory was supported by the U. S. Department of Energy, Office of Science, Office of Basic Energy Sciences, under Contract No. DE-AC02-06CH11357.

Figure Captions

Figure 1: Comparison of XRD patterns of (a) typical $LiFeBO_3$ with impurities, (b) high-purity $LiFeBO_3$ and (c) $LiFeBO_3$ simulated from ref. ICSD94317. Green bars represent the expected Bragg peak positions, blue diamond symbols refer to Fe_3BO_5 impurity and red dots refer to $LiBO_2$.

Figure 2: Rietveld refinements of $LiFeBO_3$ (Synchrotron 11-BM) χ^2=1.24 R_{bragg}=6.70% Rf=4.98% R_p=10.4% R_{wp}=13.5%. The Fe impurity(*) content is around 0.5% by weight. The red dots correspond to experimental data, black line is the calculated fit and the blue line is the difference between calculated and observed patterns. The vertical green sticks represent the expected positions of Bragg peaks. Selected enlarged regions show resolution comparison between laboratory X-ray and 11-BM Synchrotron X-ray

Figure 3: (a) Monoclinic $LiFeBO_3$ crystal structure along the *a*-axis to illustrate the connectivity of edge-sharing FeO_5 trigonal bipyramids. (b) Schematic view of our model: the green ellipsoid stands for Fe atom, the two black dots inside Fe ellipsoid represent partially occupied Fe positions from Legagneur's model. (c) Local geometry of the crystal structure around the Fe atoms, and (d) Li atoms (Boron-grey, Iron-dark green, Lithium-yellow/light blue and Oxygen in red)

Figure 4: Rietveld refinements of $^{7}LiFe^{11}BO_3$ (Neutron D2B ILL) R_{bragg}=5.38% Rf=3.11% R_p=3.45% R_{wp}=4.40%. The red dots correspond to experimental data, black line is the calculated fit and the blue line is the difference between calculated and observed patterns. The vertical green sticks represent the expected positions of Bragg peaks.

Figure 5: (a) ^{6}Li MAS NMR spectra of $LiFeBO_3$ *C*2/*c*. The spectrum can be described as a sum of two contributions: Li1=-234ppm (66%), Li2=-221ppm (34%).(b) ^{6}Li MAS NMR spectra of $LiMnBO_3$ *C2/c*, the spectrum can be described as a sum of two contributions. Li1=-194ppm (65%), Li2=-209ppm (35%) with both line widths around 20ppm. Red dots represent the recorded spectrum, Li(1) contribution is labeled as green, while Li(2) contribution is labeled as blue, and black line is the sum of the two contributions.

Figure 6: (a) $LiFeBO_3$ Mossbauer Spectrum recorded at 293K and (b) at 70K. Both spectra were fitted by four Fe^{2+} environments to ensure the differences between experimental data and calculated fits are reasonable.

Figure 7: The (*h0l*) reciprocal lattice plane for $LiFeBO_3$. On the left the exposure time per image is 300 seconds, and the satellite reflections were observed. While on the right, for the same crystal no obvious superstructure peaks were noticed with a standard 30 seconds exposure time per image.

Figure 8: Charge and discharge curves for (a) $LiFeBO_3$ (huge particles, diameter~20μm, prepared by conventional ceramic method) cycled at C/50 rate, 20°C, using LP30 liquid electrolyte. Only around $0.15Li^+$ per formula could be delithiated. (b) $LiFeBO_3$/C (agglomerated carbon coated small particles, prepared by self-combustion) cycled at C/50 rate, 20°C, using LP30 liquid electrolyte. Around 0.8Li+ per formula was able to be extracted.

Figure 9: (a & b) TEM image of sample "C", and (c) charge and discharge curves for *insitu* carbon coated $LiFeBO_3$ (small particles, diameter~100nm) cycled at C/20 rate, 55^{o}C within 1.5-4.5V voltage range, using LP30 liquid electrolyte. Almost full capacity was delivered and an operating voltage of $LiFeBO_3$ ~2.8V vs Li/Li^+ was clearly demonstrated.

Figure 10: (a) Charge and discharge curves for sample (C) cycled at C/20 rate, 55^{o}C within 2.0-4.5V voltage range, using LP30 liquid electrolyte. Around 0.7 Li^+ per formula could be removed / extracted. (b) Capacity retention for the same cell, which could still deliver a capacity of 130 mAh/g at the 50th cycle.

Table 1. Crystallographic data of $LiFeBO_3$ derived from Rietveld refinements of room temperature neutron powder diffraction patterns and Selected interatomic distances (Å) and angles (deg.)

Formula	Atom	S.O.F.	x	y	z	B_{iso}(Å^2)	BVS
$LiFeBO_3$	Li(1)	0.50(3)	0.667(4)	0.510(4)	0.170(3)	0.59(23)	**1.02**(4)
C2/c	Li(2)	0.50(3)	0.705(5)	0.480(3)	0.086(3)	0.59(23)	**1.03**(4)
a = 5.1614(1)Å	Fe	1.0	0.1613(9)	0.3329(6)	0.1235(4)	anisotropic	**1.98**(2)
b = 8.9080(2)Å	B	1.0	0.165(1)	0.6662(7)	0.1246(5)	0.55(5)	**2.88**(4)
c = 10.1643(3)Å	O1	1.0	0.405(1)	0.1638(7)	0.0879(5)	0.46(7)	**2.00**(3)
β = 91.225(2)^o	O2	1.0	0.779(1)	0.3042(6)	0.1607(6)	0.89(9)	**1.98**(3)
V = 467.22(2) Å^3	O3	1.0	0.3158(1)	0.5404(4)	0.1261(7)	1.42(8)	**1.90**(3)

R_{Bragg}=5.38% R_f=3.11% R_p=3.45% R_{wp}=4.40% χ^2=6.15

anisotropic thermal parameters (Å^2)x10^{-4}

Atom	U11	U22	U33	U12	U13	U23
Fe	186 (14)	11 (10)	234 (14)	-9(16)	-162(9)	-2(18)

The form of the anisotropic thermal parameters is:
$\exp[-2\pi^2(h^2a^{*2}U_{11}+k^2b^{*2}U_{22}+l^2c^{*2}U_{33}+2hka^*b^*U_{12}+2hla^*c^*U_{13}+2klb^*c^*U_{23}]$

BO_3

	O1	***O2***	***O3***
O1	**1.387(9)**	118.7(6)	112.6(6)
O2	2.406(8)	**1.408(8)**	118.6(6)
O3	2.415(8)	2.385(7)	**1.365(8)**

$Li(1)O_4$

	O1	***O2***	***O3***	***'Axial' O3***
O1	**2.03(3)**	115.9(2)	113.2(1)	107.9(1)
O2	3.354(9)	**1.93(3)**	114.5(1)	99.4(1)
O3	3.263(9)	3.199(8)	**1.88(2)**	103.7(1)
'Axial' O3	3.331(9)	3.066(9)	3.123(9)	**2.09(3)**

$Li(2)O_4$

	O1	***O2***	***O3***	***'Axial' O3***
O1	**1.93(3)**	129.1(1)	106.8(1)	95.5(1)
O2	3.354(9)	**1.78(3)**	109.6(1)	110.9(1)
O3	3.263(9)	3.199(8)	**2.13(3)**	100.6(1)
'Axial' O3	3.037(8)	3.256(9)	3.303(9)	**2.16(3)**

FeO_5

	O1	***O2***	***O3***	***Axial O1***	***Axial O2***
O1	**1.999(8)**	123.7(3)	116.4(4)	85.2(3)	91.0(3)
O2	3.554(8)	**2.032(8)**	119.9(4)	93.1(3)	85.1(3)
O3	3.408(7)	3.502(8)	**2.012(7)**	93.1(3)	92.7(3)
Axial O1	2.824(8)	3.052(8)	3.037(8)	**2.169(7)**	174.1(3)
Axial O2	3.015(9)	2.882(9)	3.066(9)	4.385(4)	**2.222(8)**

References

1. Padhi, A.K., K.S. Nanjundaswamy, and J.B. Goodenough, Phospho‐olivines as Positive‐Electrode Materials for Rechargeable Lithium Batteries. Journal of The Electrochemical Society, 1997. **144**(4): p. 1188-1194.
2. Padhi, A.K., et al., Effect of Structure on the Fe3 + / Fe2 + Redox Couple in Iron Phosphates. Journal of The Electrochemical Society, 1997. **144**(5): p. 1609-1613.
3. Masquelier, C. and L. Croguennec, Polyanionic (Phosphates, Silicates, Sulfates) Frameworks as Electrode Materials for Rechargeable Li (or Na) Batteries. Chemical Reviews, 2013.
4. Nishimura, S.-i., et al., Structure of Li2FeSiO4. Journal of the American Chemical Society, 2008. **130**(40): p. 13212-13213.
5. Sirisopanaporn, C., Structural and electrochemical properties of Li_2MSiO_4 (M = Fe, Mn) cathode materials for Li-ion batteries. Ph.D. Dissertation Université de Picardie Jules Verne - Univerza v Ljubljani, 2011: p. 21.
6. Islam, M.S., et al., Silicate cathodes for lithium batteries: alternatives to phosphates? Journal of Materials Chemistry, 2011. **21**(27): p. 9811-9818.
7. Recham, N., et al., A 3.6[thinsp]V lithium-based fluorosulphate insertion positive electrode for lithium-ion batteries. Nat Mater, 2010. **9**(1): p. 68-74.
8. Tripathi, R., et al., Scalable Synthesis of Tavorite LiFeSO4F and NaFeSO4F Cathode Materials. Angewandte Chemie International Edition, 2010. **49**(46): p. 8738-8742.
9. Barpanda, P., et al., A 3.90 V iron-based fluorosulphate material for lithium-ion batteries crystallizing in the triplite structure. Nat Mater, 2011. **10**(10): p. 772-779.
10. Rowsell, J.L.C., J. Gaubicher, and L.F. Nazar, A new class of materials for lithium-ion batteries: iron(III) borates. Journal of Power Sources, 2001. **97–98**(0): p. 254-257.
11. Ibarra-Palos, A., et al., Electrochemical Reactions of Iron Borates with Lithium: Electrochemical and in Situ Mössbauer and X-ray Absorption Studies. Chemistry of Materials, 2002. **14**(3): p. 1166-1173.
12. Okada, S., et al., Anode properties of calcite-type MBO3 (M:V, Fe). Journal of Power Sources, 2003. **119–121**(0): p. 621-625.
13. Rowsell, J.L.C. and L.F. Nazar, Synthesis, structure, and solid-state electrochemical properties of CrBO: a new chromium() borate with the norbergite structure. Journal of Materials Chemistry, 2001. **11**(12): p. 3228-3233.
14. Débart, A., et al., Study of the Reactivity Mechanism of M3B2O6 (with M = Co, Ni, and Cu) toward Lithium. Chemistry of Materials, 2003. **15**(19): p. 3683-3691.
15. Legagneur, V., et al., LiMBO3 (M=Mn, Fe, Co):: synthesis, crystal structure and lithium deinsertion/insertion properties. Solid State Ionics, 2001. **139**(1–2): p. 37-46.
16. Mba, J.-M.A., et al., Lithium Insertion or Extraction from/into Tavorite-Type LiVPO4F: An In Situ X-ray Diffraction Study. Journal of The Electrochemical Society, 2012. **159**(8): p. A1171-A1175.
17. Ateba Mba, J.-M., et al., Synthesis and Crystallographic Study of Homeotypic LiVPO4F and LiVPO4O. Chemistry of Materials, 2012. **24**(6): p. 1223-1234.
18. Allen, J.L., et al., LiMBO3 (M=Fe, Mn): Potential Cathode for Lithium Ion Batteries. MRS Online Proceedings Library, 2002. **730**: p. null-null.
19. A. Abouimrane, M.A., N. Ravet, Carbon Nano-Painting: Application to non-Phosphate Oxyanions, e.g., Borates. Proc. Electrochem. Soc., 2003. **2003-20**: p. 15.
20. Yamada, A., et al., Lithium Iron Borates as High-Capacity Battery Electrodes. Advanced Materials, 2010. **22**(32): p. 3583-3587.
21. Yamada, A., et al., Synthesis and electrochemistry of monoclinic Li(MnxFe1-x)BO3: a combined experimental and computational study. Journal of Materials Chemistry, 2011. **21**(29): p. 10690-10696.

22. *Bo, S.-H., et al., Degradation and (de)lithiation processes in the high capacity battery material LiFeBO3. Journal of Materials Chemistry, 2012.* ***22****(18): p. 8799-8809.*
23. *Dong, Y.Z., et al., The structure and electrochemical performance of LiFeBO3 as a novel Li-battery cathode material. Electrochimica Acta, 2008.* ***53****(5): p. 2339-2345.*
24. *Chen, L., et al., Structure and electrochemical properties of LiMnBO3 as a new cathode material for lithium-ion batteries. Journal of Alloys and Compounds, 2010.* ***494****(1–2): p. 415-419.*
25. *Kim, J.C., et al., Synthesis and Electrochemical Properties of Monoclinic LiMnBO3 as a Li Intercalation Material. Journal of The Electrochemical Society, 2011.* ***158****(3): p. A309-A315.*
26. *Seo, D.-H., et al., First-principles study on lithium metal borate cathodes for lithium rechargeable batteries. Physical Review B, 2011.* ***83****(20): p. 205127.*
27. *O. S. Bondareva, M.A.S., Y. K. Egorov-Tismenko, N.V. Belov, Sov. Phys. Crystallogr., 1978.* ***23****: p. 269.*
28. *Janssen, Y., et al., Structural Modulation in the High Capacity Battery Cathode Material LiFeBO3. Journal of the American Chemical Society, 2012.* ***134****(30): p. 12516-12527.*
29. *Barpanda, P., et al., High-Throughput Solution Combustion Synthesis of High-Capacity LiFeBO3 Cathode. Journal of The Electrochemical Society, 2013.* ***160****(5): p. A3095-A3099.*
30. *Moore, J.J. and H.J. Feng, Combustion synthesis of advanced materials: Part I. Reaction parameters. Progress in Materials Science, 1995.* ***39****(4–5): p. 243-273.*
31. *Tao, L., et al., Magnetic Structures of $LiMBO_3$ (M = Mn, Fe, Co) lithiated transition metal borates. Inorganic Chemistry (accepted), 2013.*
32. *Rietveld, H.M., J. Appl. Crystallogr., 1969.* ***2****: p. 65.*
33. *Rodriguez-Carvajal, J., J. Physica B, 1993.* ***192****: p. 55.*
34. *Sheldrick, G., A short history of SHELX. Acta Crystallographica Section A, 2008.* ***64****(1): p. 112-122.*
35. *Morcrette, M., et al., In situ X-ray diffraction techniques as a powerful tool to study battery electrode materials. Electrochimica Acta, 2002.* ***47****(19): p. 3137-3149.*
36. *Altomare, A., et al., EXPO2009: structure solution by powder data in direct and reciprocal space. Journal of Applied Crystallography, 2009.* ***42****(6): p. 1197-1202.*
37. *Brown, I.D. and R.D. Shannon, Acta Crystallographica, 1973.* ***A26****: p. 266.*
38. *Kim, J., et al., Linking Local Environments and Hyperfine Shifts: A Combined Experimental and Theoretical 31P and 7Li Solid-State NMR Study of Paramagnetic Fe(III) Phosphates. Journal of the American Chemical Society, 2010.* ***132****(47): p. 16825-16840.*
39. *Mali, G., et al., Li2FeSiO4 Polymorphs Probed by 6Li MAS NMR and 57Fe Mössbauer Spectroscopy. Chemistry of Materials, 2011.* ***23****(11): p. 2735-2744.*
40. *Vanderhart, D.L., W.L. Earl, and A.N. Garroway, Resolution in 13C NMR of organic solids using high-power proton decoupling and magic-angle sample spinning. Journal of Magnetic Resonance (1969), 1981.* ***44****(2): p. 361-401.*
41. *Mali, G., A. Meden, and R. Dominko, 6Li MAS NMR spectroscopy and first-principles calculations as a combined tool for the investigation of Li2MnSiO4 polymorphs. Chemical Communications, 2010.* ***46****(19): p. 3306-3308.*
42. *Mali, G., et al., Understanding (6)Li MAS NMR spectra of Li(2)MSiO(4) materials (M = Mn, Fe, Zn). Solid State Nucl Magn Reson, 2012.* ***42****: p. 33-41.*
43. *Morgan, D., A. Van der Ven, and G. Ceder, Li Conductivity in Li x MPO 4 (M = Mn , Fe , Co , Ni) Olivine Materials. Electrochemical and Solid-State Letters, 2004.* ***7****(2): p. A30-A32.*
44. *Ellis, B.L., et al., Crystal Structure and Electrochemical Properties of A2MPO4F Fluorophosphates (A = Na, Li; M = Fe, Mn, Co, Ni)†. Chemistry of Materials, 2009.* ***22****(3): p. 1059-1070.*

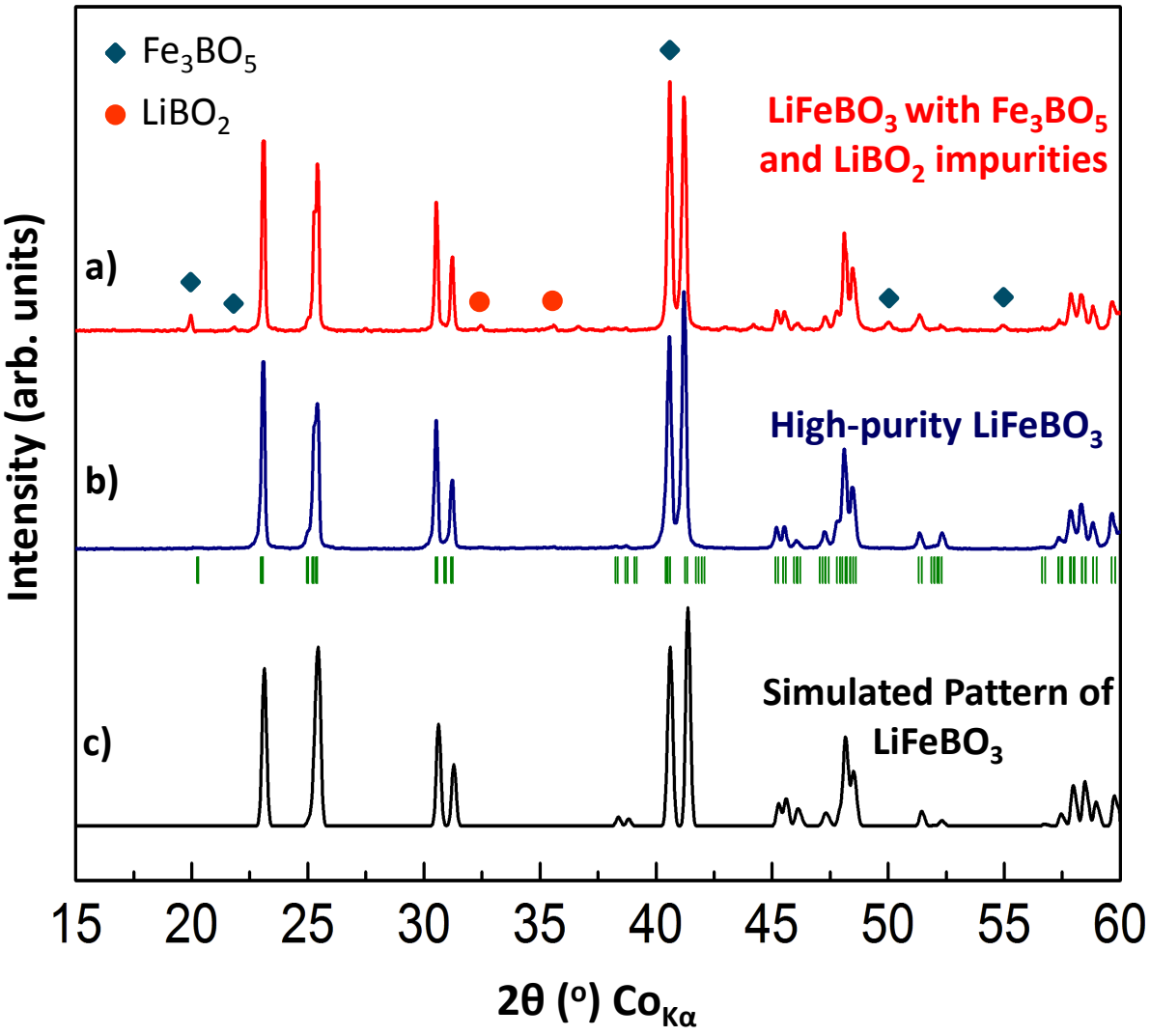

L. Tao et al., fig. 2

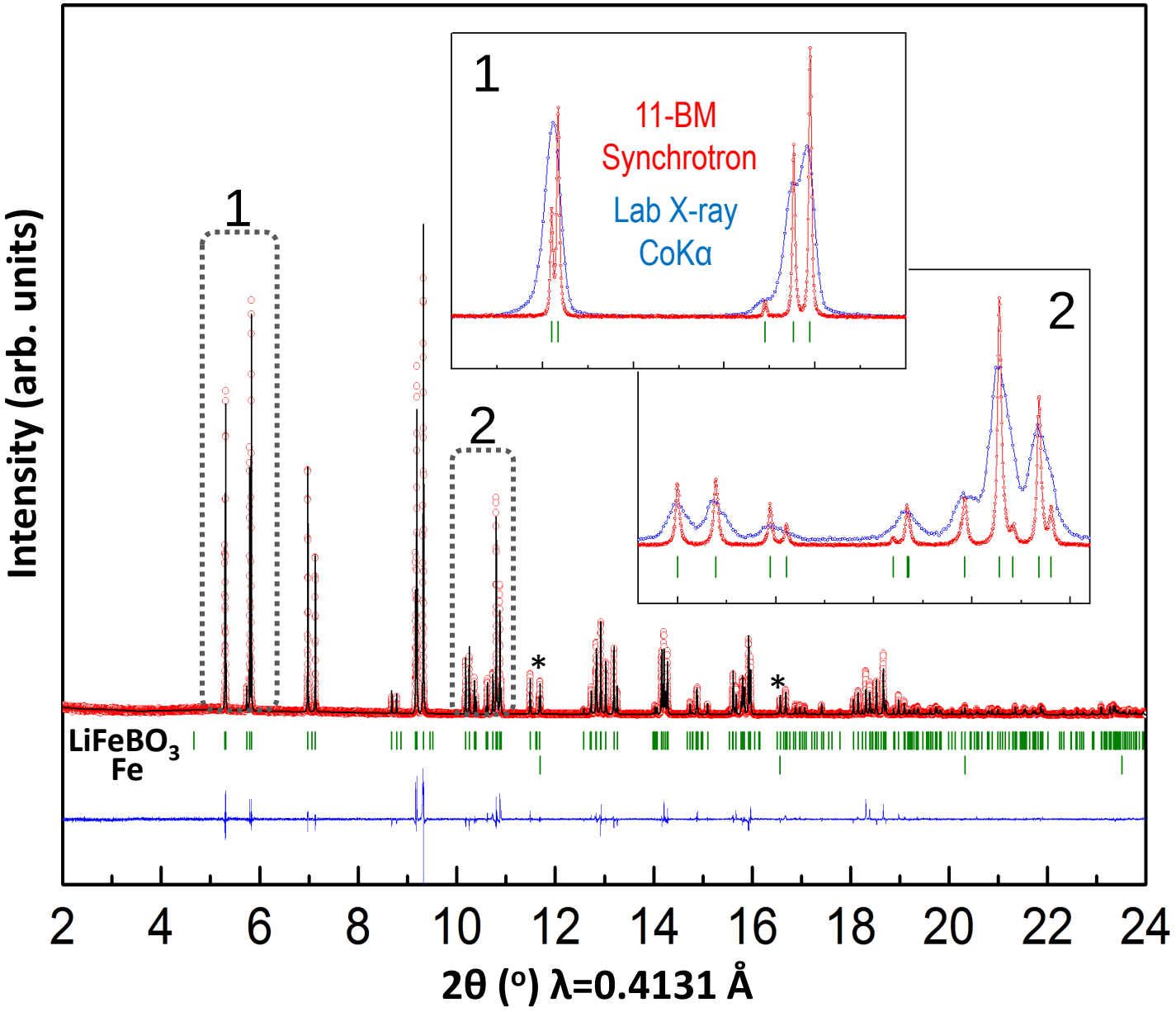

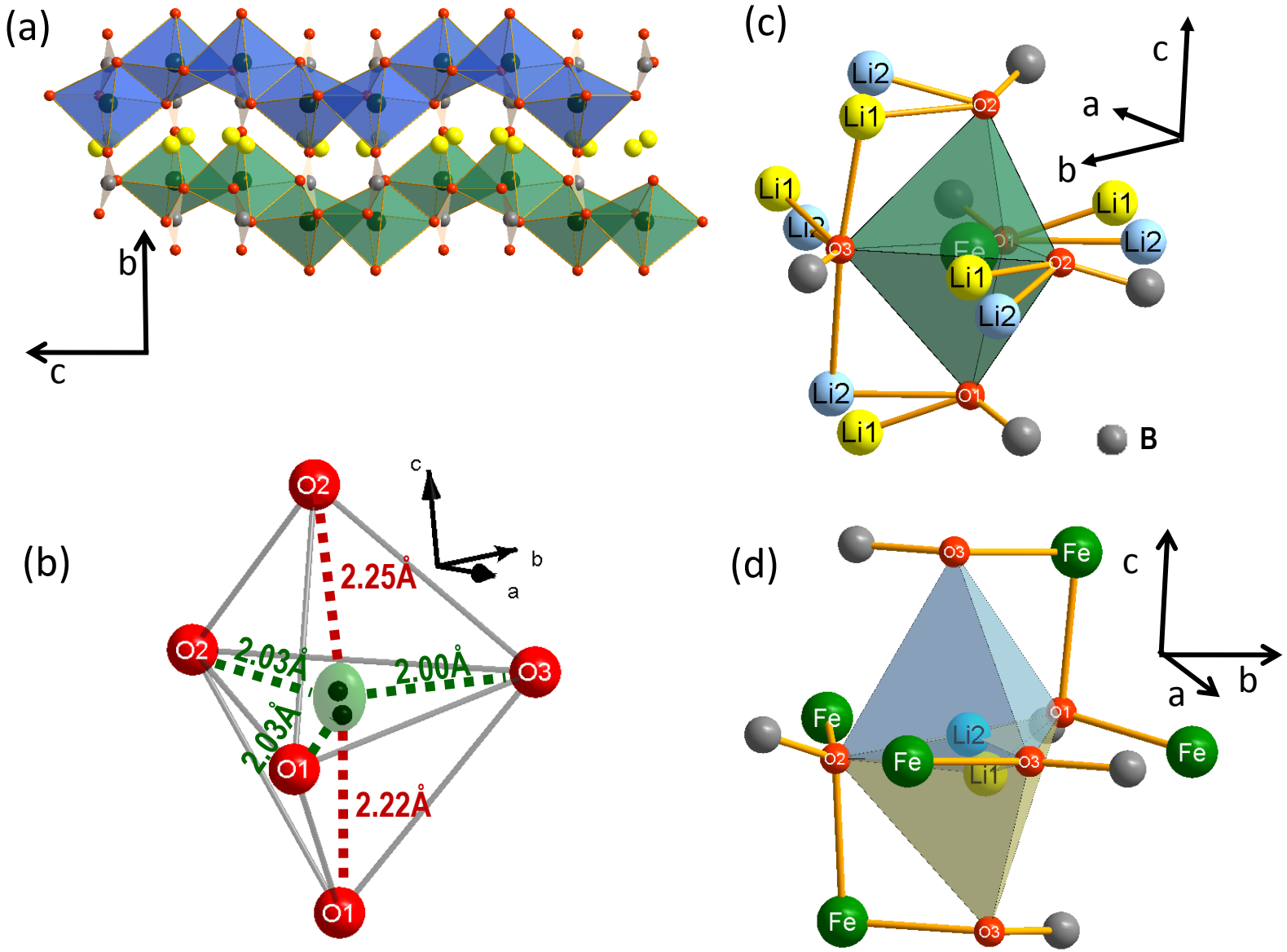

L. Tao et al., fig. 4

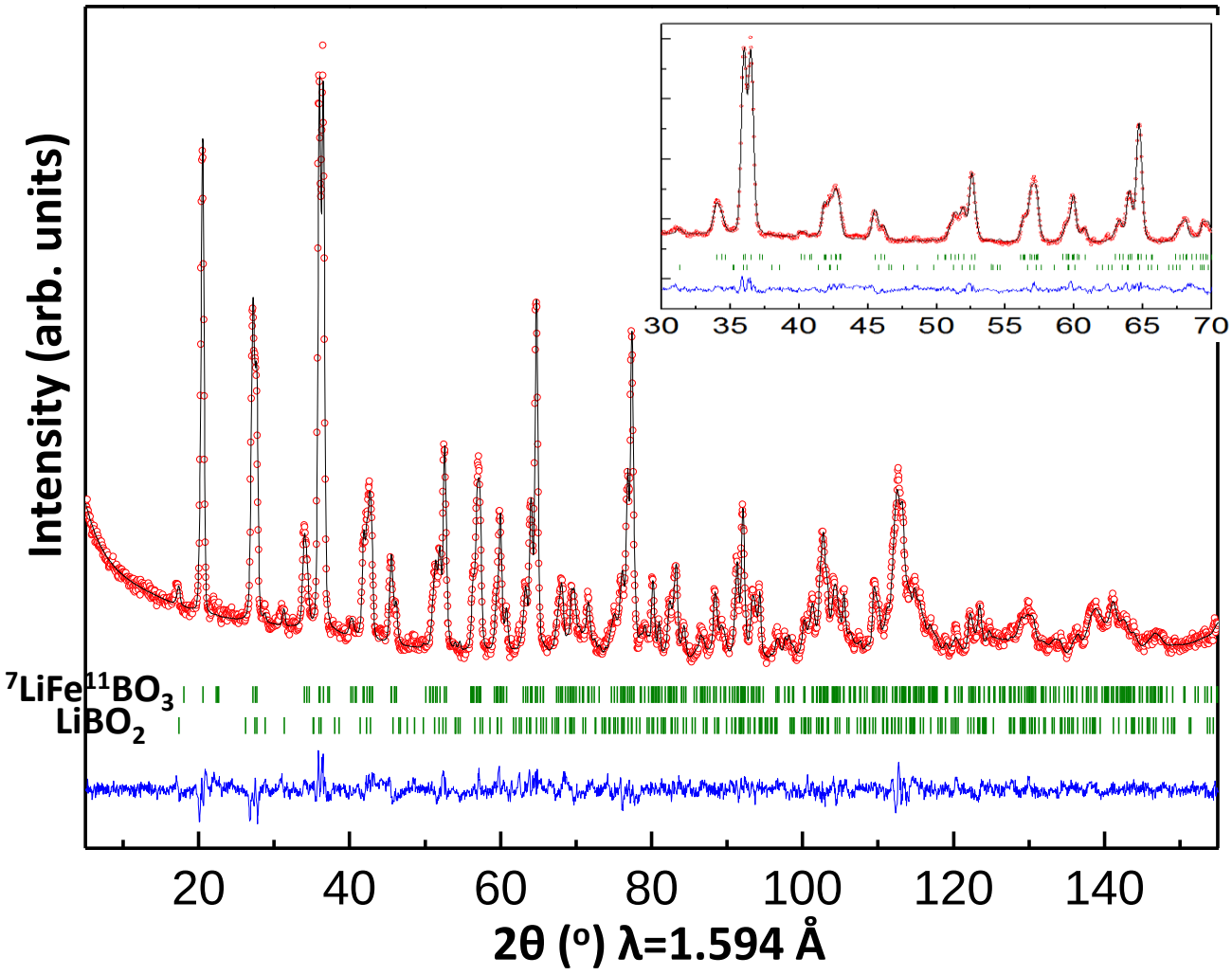

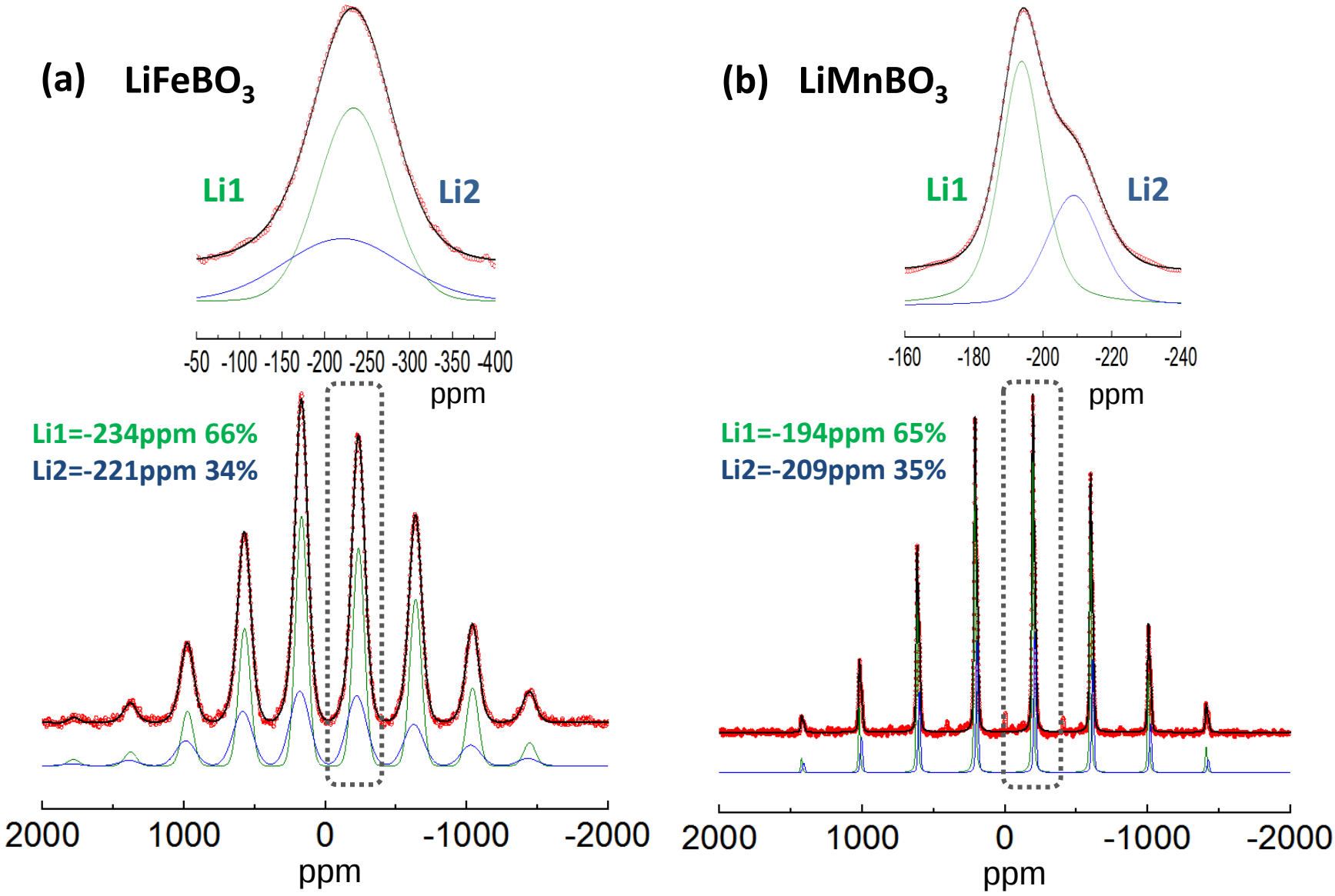

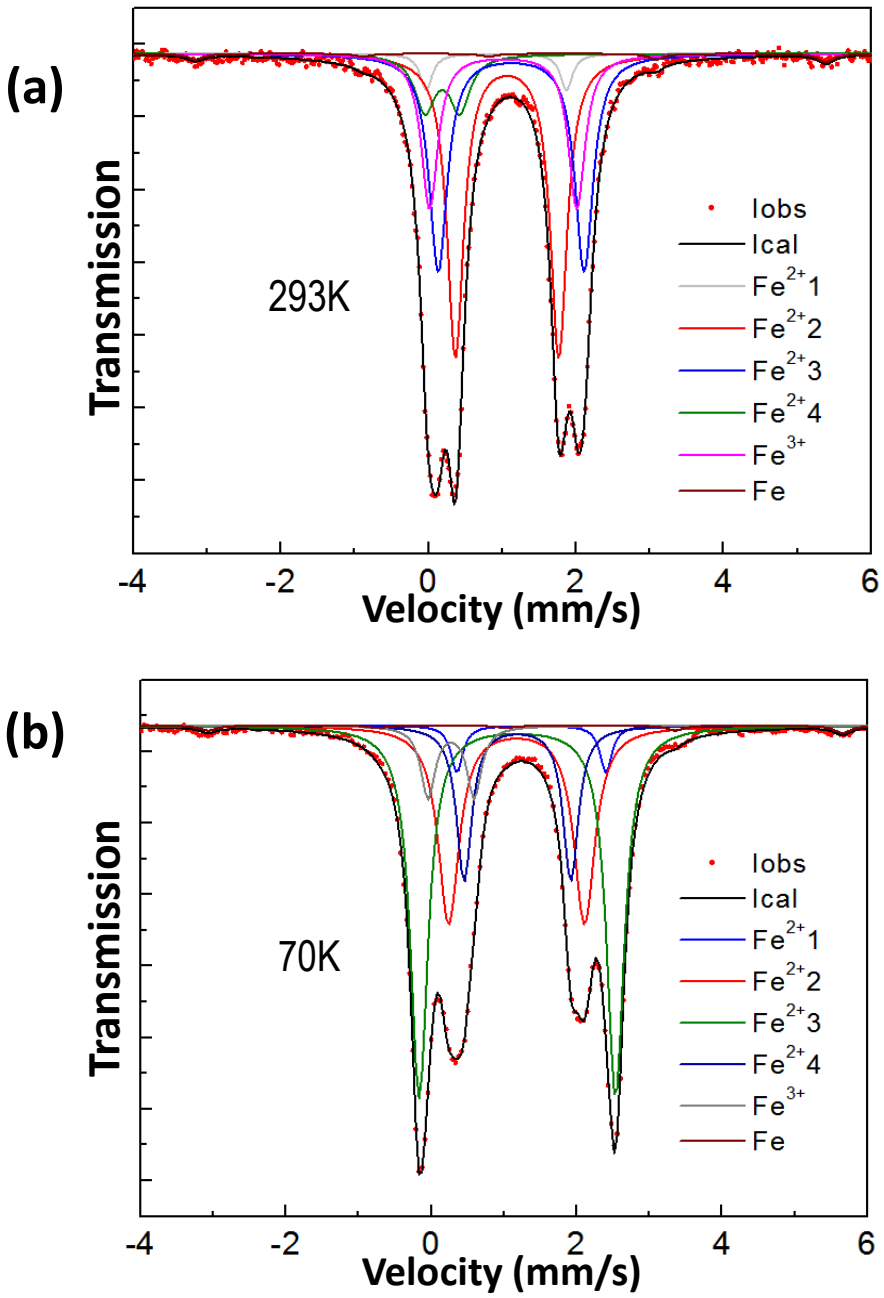

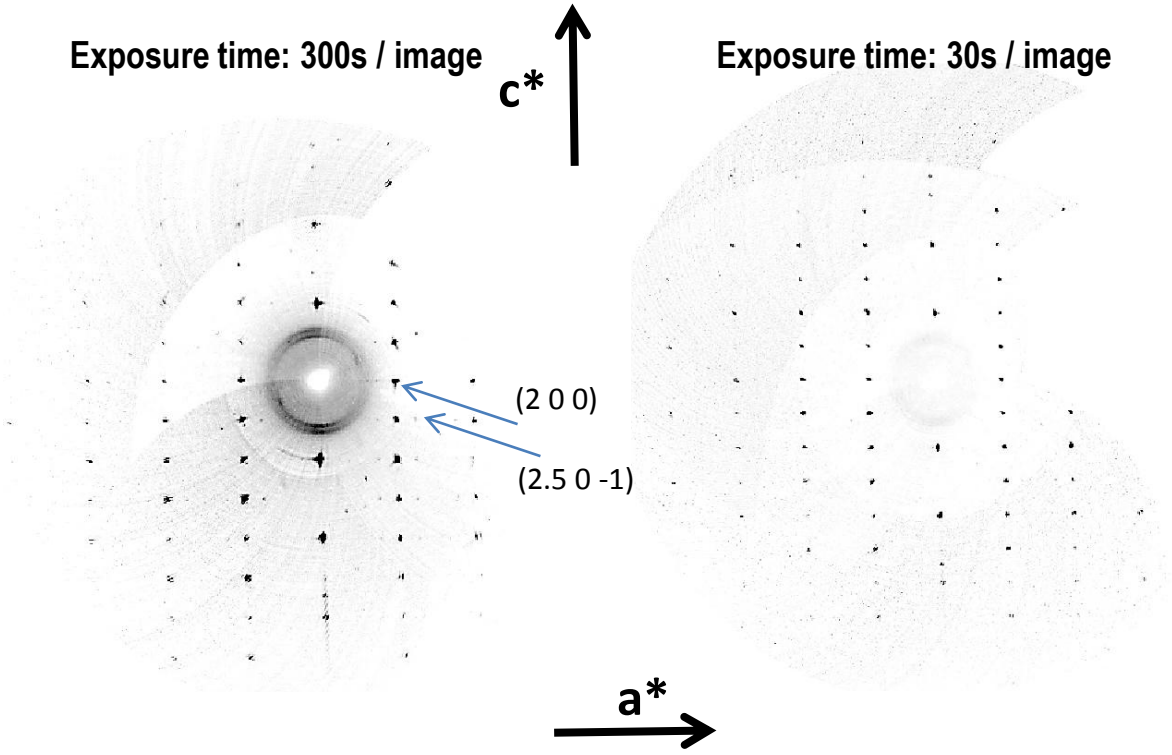

L. Tao et al., fig. 8

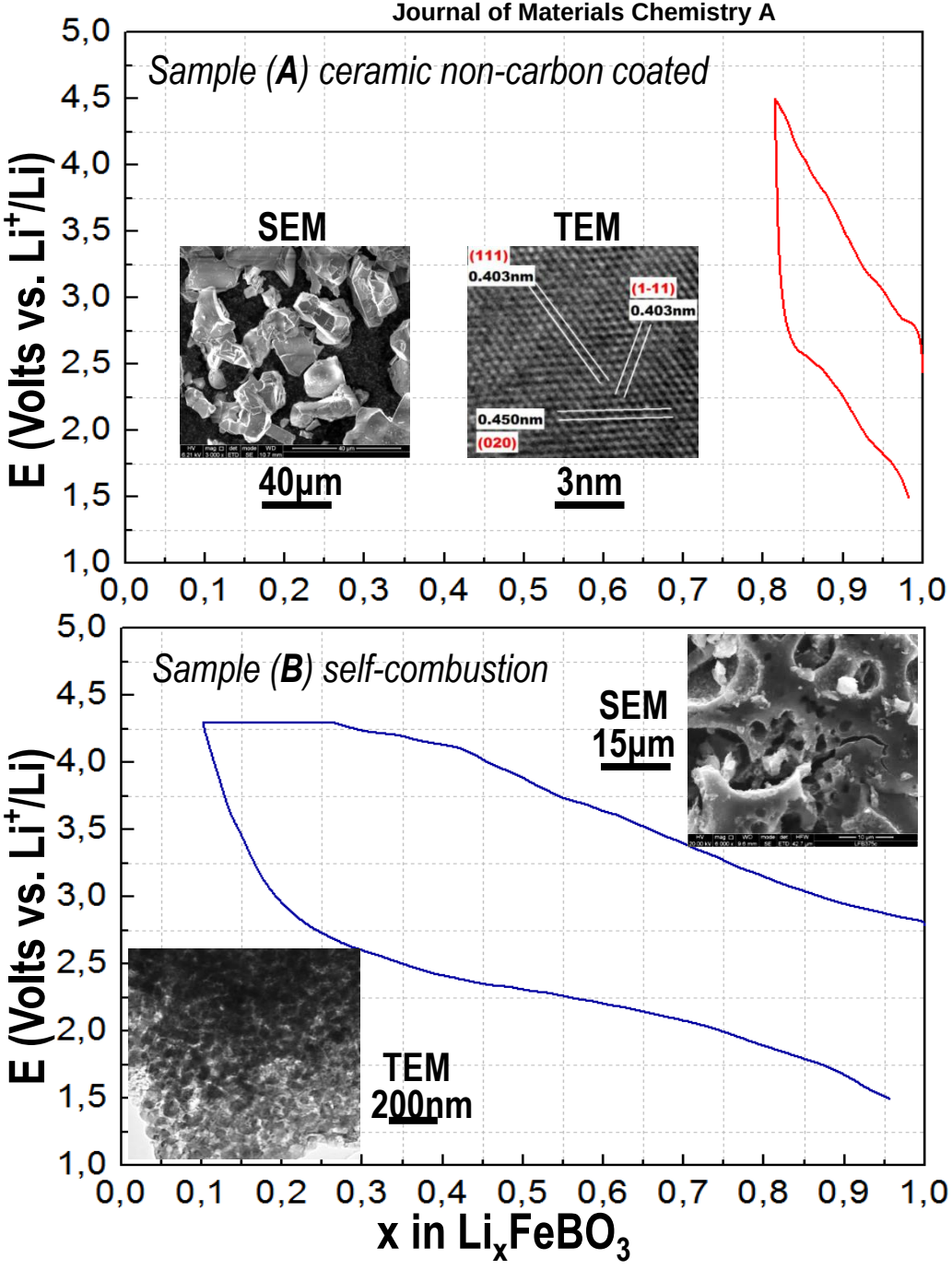

L. Tao et al., Fig. 3

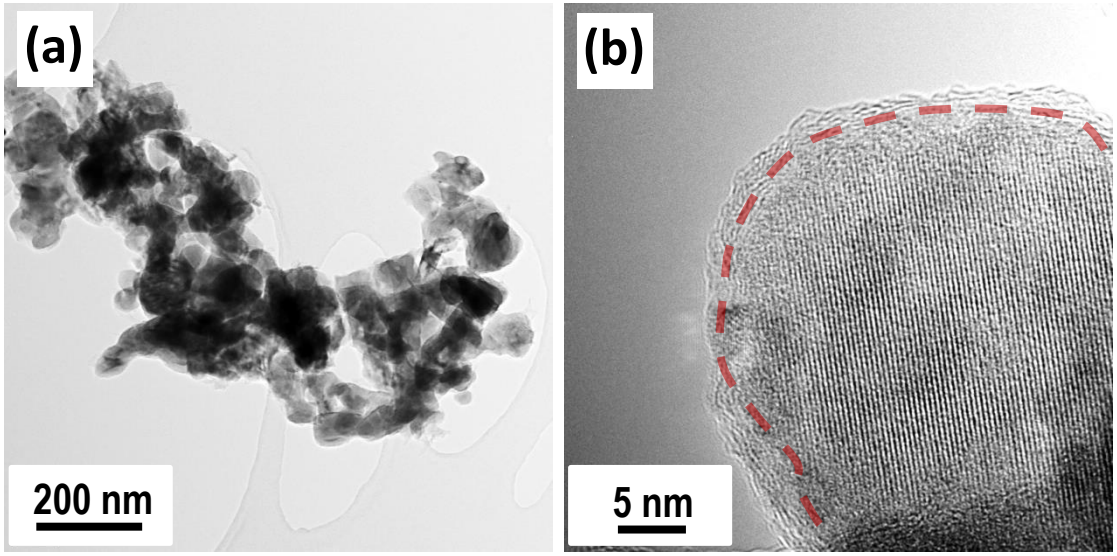

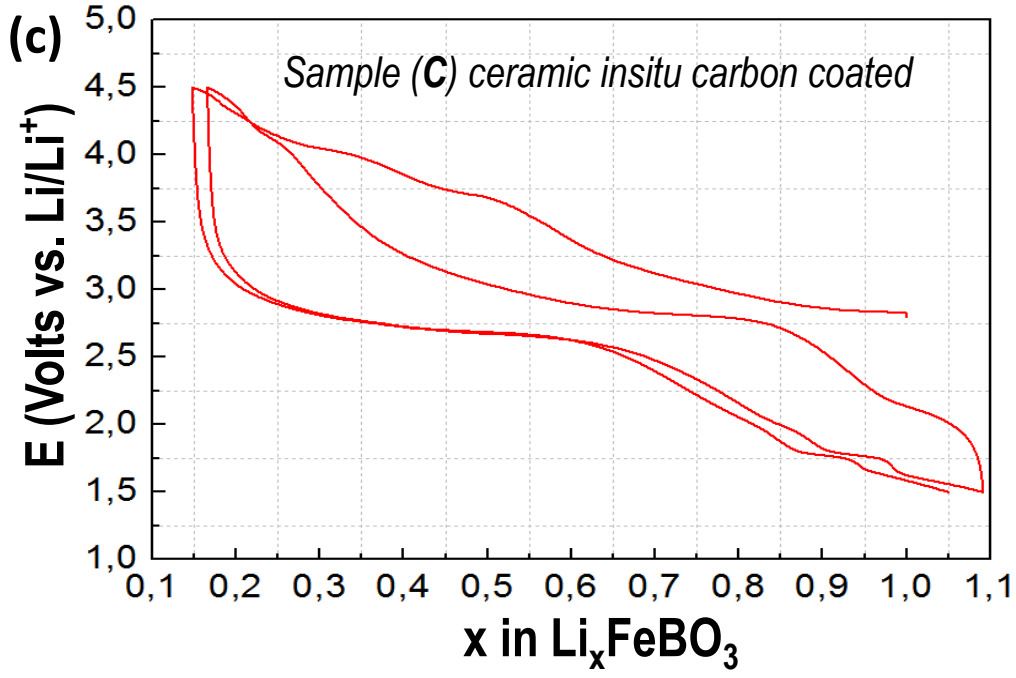

L. Tao et al., fig. 10